

First controlled vertical flight of a biologically inspired microrobot

This content has been downloaded from IOPscience. Please scroll down to see the full text.

2011 Bioinspir. Biomim. 6 036009

(<http://iopscience.iop.org/1748-3190/6/3/036009>)

View [the table of contents for this issue](#), or go to the [journal homepage](#) for more

Download details:

IP Address: 132.174.255.3

This content was downloaded on 06/03/2014 at 04:59

Please note that [terms and conditions apply](#).

First controlled vertical flight of a biologically inspired microrobot

Néstor O Pérez-Arancibia^{1,2}, Kevin Y Ma^{1,2}, Kevin C Galloway²,
Jack D Greenberg¹ and Robert J Wood^{1,2}

¹ School of Engineering and Applied Sciences, Harvard University, Cambridge, MA 02138, USA

² Wyss Institute for Biologically Inspired Engineering, Harvard University, Boston, MA 02115, USA

E-mail: nperez@seas.harvard.edu, kevinma@seas.harvard.edu, kevin.galloway@wyss.harvard.edu,
jdgreenb@seas.harvard.edu and rjwood@eecs.harvard.edu

Received 21 May 2011

Accepted for publication 4 August 2011

Published 30 August 2011

Online at stacks.iop.org/BB/6/036009

Abstract

In this paper, we present experimental results on altitude control of a flying microrobot. The problem is approached in two stages. In the first stage, system identification of two relevant subsystems composing the microrobot is performed, using a static flapping experimental setup. In the second stage, the information gathered through the static flapping experiments is employed to design the controller used in vertical flight. The design of the proposed controller relies on the idea of treating an exciting signal as a subsystem of the microrobot. The methods and results presented here are a key step toward achieving total autonomy of bio-inspired flying microrobots.

 Online supplementary data available from stacks.iop.org/BB/6/036009/mmedia

(Some figures in this article are in colour only in the electronic version)

1. Introduction

In [1], the feasibility of flying robotic insects was empirically demonstrated. However, the control challenges that need to be solved in order to achieve total autonomy of flying microrobots are both attractive and daunting. Given the maneuverability of many flying insects, it is natural to look to biology to inspire both morphology and control strategies. Researchers have attempted to elucidate the control architecture of flying insects. It appears that the key features include a plethora of sensory information [2], selection of sensor modalities appropriate to various flight conditions [3] and a reflexive network for rapid perturbation rejection [4–6]. In parallel with the evolution of sensing and computation technologies to mimic these features, we seek to demonstrate viable flight control methodologies for these microrobots using off-board sensing and computation. This is an intrinsically multidisciplinary problem, in which several engineering aspects must be considered simultaneously, including aerodynamics, sensing, actuator design, micro-fabrication and system identification for control. In this paper, we constrain the problem to one degree of freedom, namely altitude control, and in this context

we propose a framework that is also expandable to the more general case. Most significantly, we propose a methodology for synthesizing controllers that is based on a combination of analysis and experimentation. An alternative approach, not discussed here, could rely primarily on idealized modeling and simulations [7–9].

In [10] and [11], using a static single-wing flapping microrobot, a methodology for designing altitude controllers was proposed. There, the altitude control problem was transformed into the one of lift-force control, and then solved using standard system identification methods for LTI systems and a model-based adaptive control scheme. Here, we propose a two-stage methodology for tackling the problem, where in the first stage substantial *a priori* information about the system is gathered through system identification. In the second stage, the information obtained in the first stage is used as a guide for designing a feedback controller. The main idea introduced in this paper is that, as a design choice, the fundamental shape of the exciting signal applied to the microrobotic insect is selected *a priori*, based on information obtained through static flapping experiments. One way of thinking of this signal is as a basis

function. Then, some defining parameter of the chosen signal is modified in real-time according to a feedback law. This is a fairly general idea and we envision substantial research in this direction in the near future. In the case presented here, we choose sinusoidal exciting signals with fixed frequencies and varying amplitudes. This approach allows one to think of a unit sinusoidal signal as a subsystem and to think of the pre-multiplier (i.e. amplitude) as the input to the system to be controlled, whose output is the altitude of the flying insect. While the choice of a sinusoidal basis is natural for an oscillating system operating at or near resonance, this methodology is generalizable to other periodic or aperiodic choices of basis. This approach is analogous to amplitude modulation, used by many insects to control flight forces [12, 13]. Alternatively, the amplitude can be fixed and the flapping frequency varied for frequency modulation [12, 13].

In the context of this research, progress is achieved through a constant interaction between mechanical design and controller design. While the main mechanical features of the microrobot are inspired by nature, they are designed and fabricated to be compatible with the implementation of the control strategies we develop. Similarly, the control algorithms are inspired by nature but constrained by the microrobotic system capabilities. Thus, the resulting solution has flavors of both bioinspiration (reflected on the discussions on amplitude versus frequency modulation for thrust control [13] and the use of active versus passive wing rotation to manipulate flight forces [14, 15]) and classical control techniques.

The developments presented in this paper are a key step in achieving the goal of autonomous flying microrobots. A main result is that stable hovering and vertical trajectory following are achievable with an under-actuated system that relies on passive wing motions during operation [16]. This is the first demonstration of closed-loop control of an insect-scale robot. A second significant result is that the robotic insect in figure 1 is capable of generating lift-forces as much as 3.6 times its weight. This provides room for payload such as steering actuators and structures [17], sensors and power. The forthcoming sections describe the methodology for developing controllers for flying flapping-wing robotic insects and present compelling evidence on the viability of the proposed approach with experiments on a 56 mg robot (see figure 1).

Notation

- As usual, \mathbb{R} and \mathbb{Z}^+ denote the sets of real and non-negative integer numbers, respectively.
- The variable t is used to index discrete time, i.e. $t = \{kT_s\}_{k=0}^{\infty}$ with $k \in \mathbb{Z}^+$ and $T_s \in \mathbb{R}$. As usual, T_s is referred to as the sampling-and-hold time.
- The variable τ is used to index continuous time. Thus, for a generic continuous-time variable $x(\tau)$, $x(t)$ is the sampled version of $x(\tau)$.
- z^{-1} denotes the delay operator, i.e. for a signal x , $z^{-1}x(k) = x(k-1)$ and conversely $zx(k) = x(k+1)$. For convenience, z is also the complex variable associated with the z -transform.

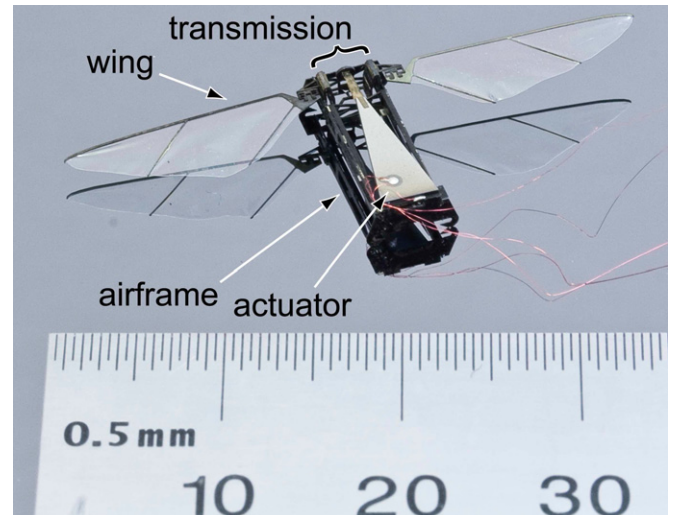


Figure 1. Photograph of the biologically inspired microrobotic flying insect.

2. Experiments and controller design

2.1. Problem formulation

The final goal of our research efforts is to design and control a flapping-wing flying microrobot, similar to the one in figure 1, capable of sustained autonomous flight. As shown in figure 2, the device in figure 1 is unstable in open loop. This microrobot was designed such that drag forces are symmetric about the upstroke and downstroke, summing to 0, and the mean lift force vector intersects the center of mass. Thus, ideally, no body torques are generated and the angles of rotation in three dimensions about the robot's center of mass (pitch, roll and yaw) should stay at 0° . However, any asymmetry in the flapping mechanism, due to small fabrication errors, would cause the robot to deviate from the vertical trajectory. The solution of this problem requires the incorporation of additional actuators to the robot's design, since the model described here is under-actuated. This topic is a matter of current research [17]. Here, we concentrate on the control of a single degree of freedom: altitude.

The specific objective of the research presented in this paper is the invention and implementation of an altitude control strategy for the microrobot in figure 1 constrained to move along a vertical axis. The analysis begins with the free body diagram of the microrobot shown in figure 3. A first thing to note is that from figure 3, the equation of motion along the vertical axis is simply

$$\gamma_L(\tau) - mg = m\ddot{x}(\tau), \quad (1)$$

where m is the mass of the robot, g is the gravitational acceleration and $\gamma_L(\tau)$ is the instantaneous lift force generated by the flapping wings. In some cases, an additional dissipative body drag term $\kappa_d \dot{x}(\tau)$ could be added to the right side of (1), where κ_d is a constant to be identified experimentally. Note that the system, as described by (1), is unstable because its input-output representation has two poles at 0. As described in [10, 11] and [16], the lift force $\gamma_L(\tau)$ is a nonlinear

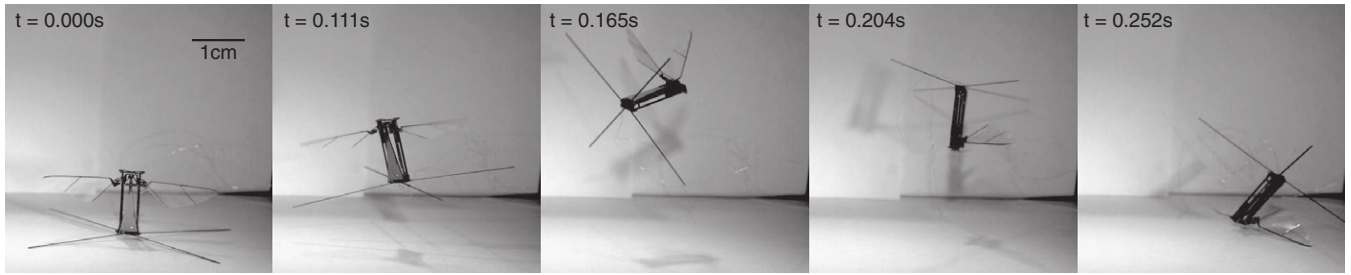


Figure 2. Video sequence of an unconstrained free flight experiment used to highlight the need for an active control strategy. Here, the under-actuated microrobotic fly in figure 1 is powered in open loop, and then it takes off and remains airborne until crashing due to its intrinsically unstable behavior.

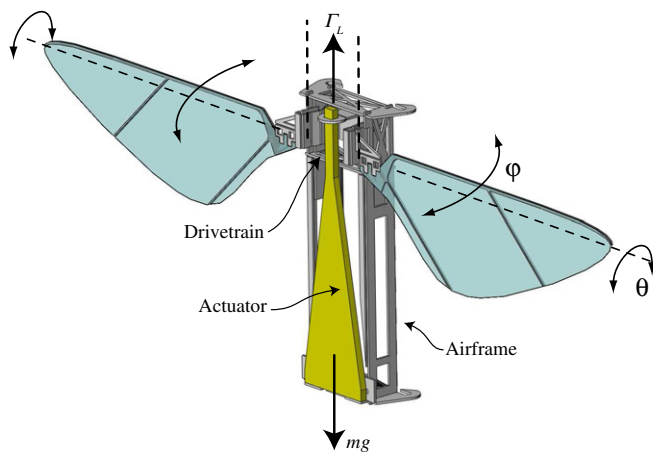


Figure 3. Illustration of the microrobotic fly employed in the research presented in this paper, similar to the one in [1]. This microrobot was entirely designed and fabricated by the authors at the Harvard Microrobotics Laboratory. Γ_L : average lift force; φ : flapping angle (also referred to as stroke angle); θ : passive rotation angle.

function of the frequency and amplitude of the flapping angle φ . Also as discussed in [10], [11] and [16], for sinusoidal inputs, instantaneous lift forces $\gamma_L(\tau)$ typically oscillate around some non-zero mean force, crossing zero periodically. Therefore, ascent occurs when the average lift force is larger than mg .

In some studies of biological flapping-flight [12, 18, 19], the mean total force, Φ_T , generated by a wing (or a symmetrical wing pair) throughout the stroke is estimated as

$$\Phi_T = \int_0^{\Xi} \rho \bar{C}_\phi \bar{v}_r^2(\xi) c(\xi) d\xi, \quad (2)$$

which is a standard quasi-steady blade-element formulation of flight force (see [16] and references therein), where ρ is the density of the air (1.2 kg m^{-3} , [12]), \bar{C}_ϕ is the mean force coefficient of the wing throughout the stroke, $\bar{v}_r^2(\xi)$ is the mean square relative velocity of each wing section, $c(\xi)$ is the chord length of the wing at a distance ξ from the base, and Ξ is the total wing length. Note that assuming a horizontal stroke plane, for a sinusoidal stroke $\varphi(\tau) = \varphi_0 \sin(2\pi f_r \tau)$, the relative velocity of the wing section can be estimated as

$$v_r(\tau, \xi) = \xi \dot{\varphi}(\tau) = 2\pi f_r \xi \varphi_0 \cos(2\pi f_r \tau), \quad (3)$$

which implies that the mean square relative velocity of each wing section can be roughly estimated as

$$\bar{v}_r^2(\xi) = 4\pi^2 f_r^2 \xi^2 \varphi_0^2 \frac{1}{T_r} \int_0^{T_r} \cos^2(2\pi f_r \tau) d\tau, \quad (4)$$

with $T_r = f_r^{-1}$. Thus, it immediately follows that

$$\bar{v}_r^2(\xi) = 2\pi^2 \xi^2 \varphi_0^2 f_r^2, \quad (5)$$

which implies that regardless of the size and shape of the wing (or symmetrical wing pair), the estimated mean total flight force directly depends on f_r^2 and φ_0^2 . This indicates that in order for flying insects to accelerate against gravity or hover at a desired altitude, they can modulate the average lift force by changing the stroke amplitude, φ_0 , or by changing the stroke frequency, f_r . The first technique is referred to as *amplitude modulation* and the second as *frequency modulation*.

In the problem considered here, the model in (2) is not practical for designing a general control strategy, because it explicitly depends on the morphology of the particular system to be controlled. However, we can use (5) as a general guideline from which we can inspire control strategies. In the robots considered here, the transmission that maps the actuator output, $y(t)$, to the stroke angle, $\varphi(t)$, can be approximated by a constant κ_T , i.e. $\varphi(t) = \kappa_T y(t)$. Thus, changing the amplitude and/or the frequency of $y(t)$, Φ_T can be modulated. The control strategies proposed here can be used for amplitude modulation or frequency modulation. However, we mostly concentrate on amplitude modulation.

As shown in figure 3, in this case, lift forces are generated through passive rotation. This means that there is not an active mechanism rotating the wings around their respective wing hinges. Instead, the rotation θ in figure 3 is produced by inertial forces and by the dynamic interaction of the wings with the air. The rotation θ is essential, since without it, the wings would not face the air with the angles of attack required for the generation of lift forces. In contrast to the case considered in this paper, in nature, the wing rotations necessary for creating angles of attack seem to be produced by a combination of active and passive mechanisms that cause the wings not only to rotate, but also to deform [14, 15].

When using digital computers for measurement and control, $\gamma_L(\tau)$ will be sampled at a fixed sampling rate T_s .

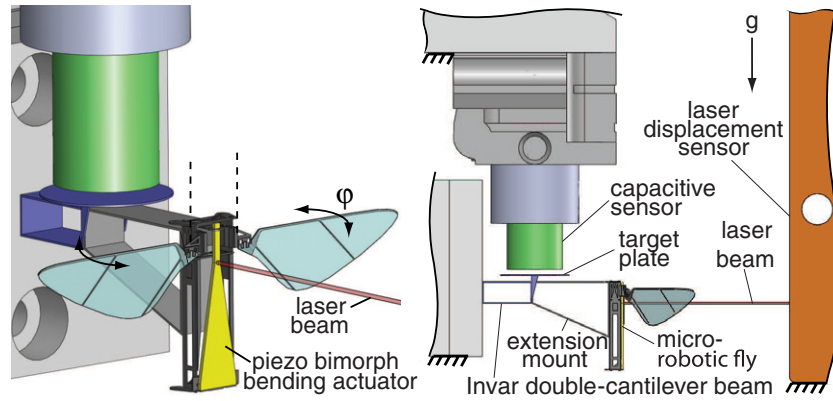


Figure 4. Setup used in static flapping experiments. Left: isometric view. Right: side view. Here, the flapping microrobot is attached to an Invar double-cantilever beam, whose deflection is measured by a capacitive displacement sensor. This deflection is proportional to the instantaneous lift force generated by the wing flapping. The deformation of the actuator is measured using a CCD laser displacement sensor. For further details, see subsection 5.4.

The sampled discrete-time version of $\gamma_L(\tau)$ is labeled as $\gamma_L(t)$. Therefore, the average lift force can be estimated as

$$\Gamma_L^{(N_L)}(t) = \Gamma_L^{(N_L)}(kT_s) = \Gamma_L^{(N_L)}(k) = \frac{1}{N_L} \sum_{i=0}^{N_L-1} \gamma_L(k-i), \quad (6)$$

where $0 < N_L \in \mathbb{Z}^+$. Often, the superscript (N_L) will be dropped and we will simply write $\Gamma_L(t)$, if N_L is obvious from the context. Note that for an ascending or hovering robotic fly, $\Gamma_L(t)$ is an estimate of Φ_T . Thus, as previously described in [10] and [11], the original altitude control problem can be translated into one of discrete-time average lift force tracking, and then, into one of actuator displacement output signal following. These topics are addressed in the next two subsections.

2.2. Static flapping experiments

In the rest of this section, we describe the design methodology for control strategies that enable flying microrobots to fly in a predictable manner along the vertical axis. The microrobot employed in the experiments, shown in figure 1, is an under-actuated robot capable of generating lift-forces by flapping two mechanically coupled identical wings. A complete understanding of this system based on first principles is extremely challenging because the dynamics depends on complex nonlinear aerodynamics and on nonlinear transmission and actuation mappings. Also there exists a significant variation from case to case due to fabrication errors. Therefore, in parallel with thorough modeling and simulation of these components, we rely on experimental identification. In [10] and [11], using a single-wing flapping static microrobot (i.e. rigidly connected to the ground), it was shown that a substantial amount of information can be gathered through experiments such as the one depicted in figure 4. Here, the microrobot is rigidly connected to a force sensor similar to that developed in [20]. Simultaneously, a laser displacement sensor is used to measure the displacement output of the piezoelectric actuator, drawn in yellow in figure 4, employed to transduce electrical into mechanical work, similar to the one described in [21]. The linear displacement of the drive

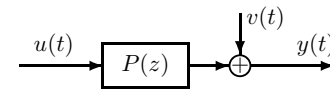


Figure 5. Idealized actuator dynamics. $P(z)$: discrete-time open-loop plant; $u(t)$: input voltage signal to the actuator; $y(t)$: output displacement of actuator; $v(t)$: output disturbance, representing the aggregated effects of all the disturbances affecting the system, including vibrations generated by the aerodynamic forces produced by the wing flapping.

actuator is mapped to an angular flapping motion employing a transmission mechanism of the type described in [1]. The resulting flapping angle is labeled by ϕ in figure 4. As explained in [16], flapping induces aerodynamic and inertial forces which produce a moment on the flexure at the wing base, generating a passive rotation that in turn creates a non-zero angle of attack during the wing stroke, thereby producing lift.

In this case, two relevant mappings can be estimated. One is the dynamic mapping from the input voltage to the actuator displacement, labeled as P , whose idealized block diagram is shown in figure 5. Here, $u(t)$ is the input, $y(t)$ is the measured output and $v(t)$ is output disturbance, representing all the disturbances affecting the system, including vibrations generated by the aerodynamic forces produced by the wing flapping. The other is the static mapping from actuator displacement to the steady-state average lift force, assuming sinusoidal displacements $y(t)$, Ψ . Thus, $\Psi(A, f) = \Gamma_L$, where A and f are the amplitude and frequency of the displacement $y(t) = A \sin(2\pi ft)$, respectively. Γ_L is the abstract steady-state average lift force produced by the flapping of the insect's wings, i.e. in (6) $N_L \rightarrow \infty$. Typically, instantaneous forces produced by the wings are oscillatory signals with a positive average value. Thus, as mentioned before, hovering occurs if Γ_L is approximately equal to the weight of the robotic insect, and vertical motion occurs if Γ_L is larger than the sum of the insect's weight and the vertical aerodynamic drag. The instantaneous force $\gamma_L(t)$ in (6) is measured with the force sensor depicted in figure 4. The transfer function P is relevant because it gives us

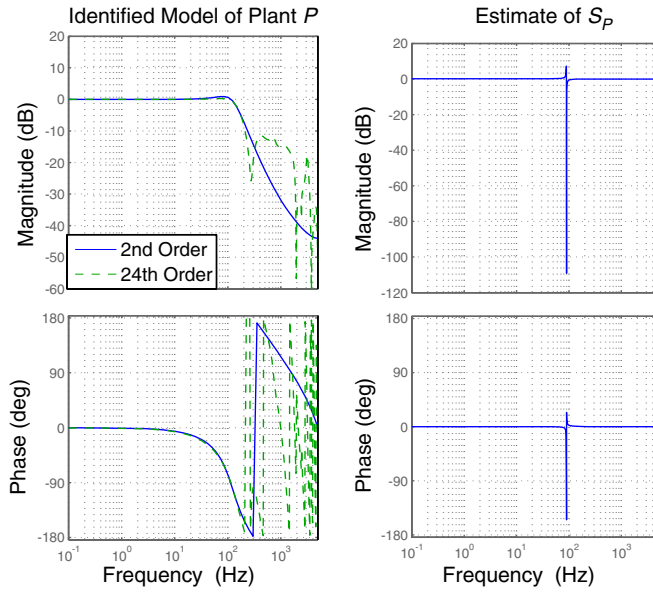


Figure 6. Left: Bode diagram of identified model $\hat{P}(z)$ of the plant $P(z)$. A 24th-order model is shown in dashed green, a reduced second-order model is shown in solid blue. Right plot: estimate $\hat{S}_P = (1 - \hat{P}Q_{90\text{Hz}})^{-1}$ of the output sensitivity function $S_P = (1 - PQ_{90\text{Hz}})^{-1}$, obtained using the LTI equivalent input–output representation of the adaptive controller used to enforce desired sinusoidal trajectories of the actuator displacement.

information about the bandwidth of the system. Also it can be used to design feedforward altitude control strategies as the one in [10] and [11]. The mapping Ψ is relevant because it allows one to choose the most suitable frequencies to drive the system.

An estimate \hat{P} of P is found using the *n4sid* algorithm [22], after exciting the system with white noise. The resulting model is shown on the left in figure 6. Note that for convenience, units are ignored and the identified models have been normalized so that the respective dc gain is 0 dB. This model is used to design an adaptive controller that enforces desired sinusoidal trajectories of the actuator, with the form $y_r(t) = A_r \sin(2\pi f_r t)$, similar to the cases shown in [10] and [11]. The main characteristic of the employed scheme is that the signal $r(t) = -y_r(t)$ is treated as an output disturbance to be rejected. This allows one to employ adaptive rejection schemes specialized in canceling families of sinusoidal signals for tracking references with the form of $y_r(t)$. As described in [10], an equivalent LTI input–output model of the adaptive scheme can be found, when the frequency f_r is fixed. This remarkable equivalence allows us to utilize classical tools to study the resulting system. This idea is shown in figure 7. The LTI equivalent output sensitivity function $S_P = (1 - PQ_{f_r})^{-1}$ can be estimated as $\hat{S}_P = (1 - \hat{P}Q_{f_r})^{-1}$, where Q_{f_r} is the LTI equivalent feedback controller for a fixed frequency f_r . Clearly S_P is the mapping from $r(t)$ to the control error $e_y(t) = y(t) + r(t)$. As an example, the resulting estimated sensitivity function, for the case $f_r = 90$ Hz, is shown on the right in figure 6. Note that a deep notch appears at 90 Hz, which implies that when $y_r(t) = A_r \sin(2\pi 90t)$, the value of $e(t)$ is essentially equal to 0, and therefore,

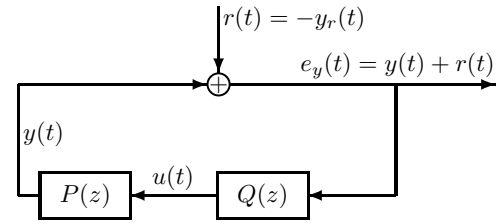


Figure 7. Block diagram of the input–output equivalent LTI model of the adaptive scheme used for following the desired displacement of the actuator $y_r(t)$, assuming $v(t) = 0, \forall t$. Here, $r(t) = -y_r(t)$ is treated as a disturbance to be rejected.

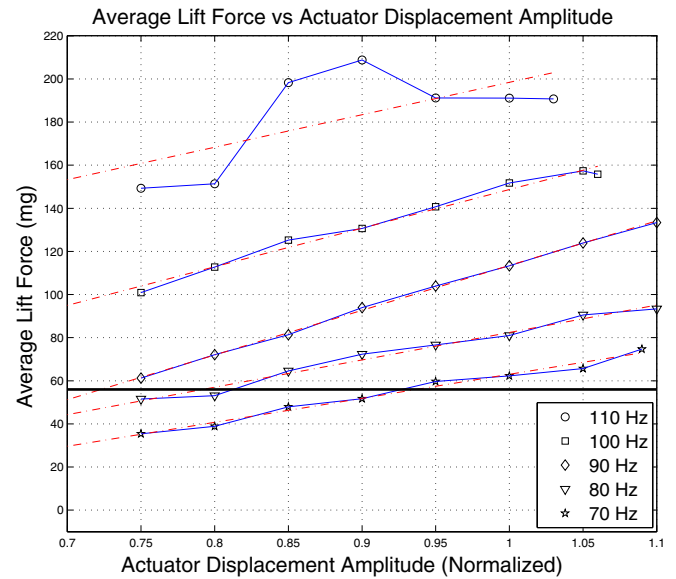


Figure 8. Empirical relationship between lift force and actuator displacement amplitude $A \approx A_r$, with f_r taking values of 70, 80, 90, 100 and 110 Hz. Here, A is normalized so that a unit input to $P(z)$, $u(t) = 1$, produces a unit output $y(t) = 1$. Also, $u(t) = 1$ means that the actuator is excited at its maximum allowable voltage 300 V. Each data point was computed from 200 000 samples, obtained at 10 kHz.

$y(t) = y_r(t)$. Thus, driving the system in closed loop, some specific points of Ψ are estimated empirically. This is done by fixing the frequency f_r , while the amplitude A_r is varied. The results are shown in figure 8, which indicate that any of the five frequencies tested, 70, 80, 90, 100 and 110 Hz, are suitable for producing lift forces capable of generating vertical motions of a 56 mg robotic insect, the case studied in this paper. The segmented red lines in figure 8 are least-squares fits to the data obtained with fixed frequencies f_r . Also shown is the 56 mg threshold which is marked using a bold black line. In figure 8, the amplitude A of the output signal $y(t) = A \sin(2\pi f t)$ is normalized so that a unit input to $P(z)$, $u(t) = 1$, produces a unit output $y(t) = 1$. Also, $u(t) = 1$ means that the actuator is excited at its maximum allowable voltage, 300 V. Each data point in figure 8 is computed from 200 000 samples, obtained at 10 kHz.

Note that the empirical relationship for the case 110 Hz is not completely linear, as it is in the other cases considered here. We do not have a definitive explanation for this anomaly. However, there are several plausible causes for the

phenomenon: (1) at this frequency, the forces exerted on the robot's airframe cause it to deform so that the mapping from the actuator displacement, $y(t)$, to the stroke angle, $\varphi(t)$, is no longer a constant, which could increase or decrease the efficiency of the mechanical transmission in unpredictable ways; (2) as explained in [1, 10, 11] and [16], lift forces are produced as the result of the passive rotation of the wings around a wing hinge. When the angle of this passive degree of freedom becomes close to $\pm 90^\circ$ (phenomenon known as over-rotation), the efficiency of the system could be substantially decreased. Over-rotation is expected to occur at relatively high flapping frequencies and amplitudes. Thus, over-rotation might explain the resulting points corresponding to $A = 0.95$, $A = 1.0$, $A = 1.05$ for the case 110 Hz; (3) higher flapping frequencies might excite undesirable resonances of the custom-made sensing mechanism, which could degrade the accuracy and precision of the static sensing device.

From figures 6 and 8, it can be inferred that one appropriate choice of drive frequency is 90 Hz, because of the large range and relatively linear relationship between amplitude and force. This follows from noting that if aerodynamic drag is neglected, in order for the robotic insect to move upward, the average lift force has to be larger than the robot's weight. And, for the robot to move downward, the robot's weight has to be larger than the generated average lift force. Therefore, a general strategy for controlling altitude emerges naturally: a feedback control law in which the control signal is the amplitude of a chosen exciting sinusoidal signal. Note that one could also choose frequency as the control signal, because of the relationship between flapping frequency and average lift force in figure 8.

It is important to mention that using the information in figure 8, a force balancing control strategy can be pursued for hovering and trajectory following. This was done in [10]. There, the controlled variable is the actuator displacement $y(t)$ and the control reference is the desired actuator displacement. The main idea is that using a look-up table found in a similar way to the one graphically described in figure 8, a desired actuator output is generated in real time, in order to produce a desired average lift force that makes the system to follow a pre-chosen vertical trajectory. As shown in [10], this strategy can be used to make the flying robot hover by balancing the robot's weight and the time-averaged lift produced by the flapping wings. As also shown in [10] using a hardware-in-the-loop experiment, trajectories can be attempted using the same approach. The problem with the balancing strategy is that this is not robustly stable. Thus, when hovering, small variations in the generated average lift forces cause the robot to slowly drift upward or downward. These problems are avoided if the altitude of the robot is directly measured and used to generate the control signal, as described in the next section.

2.3. Flight experiments

The altitude control experiment is depicted in figure 9. The experimental setup was designed to constrain the flight of the robotic insect to the vertical degree of freedom, while

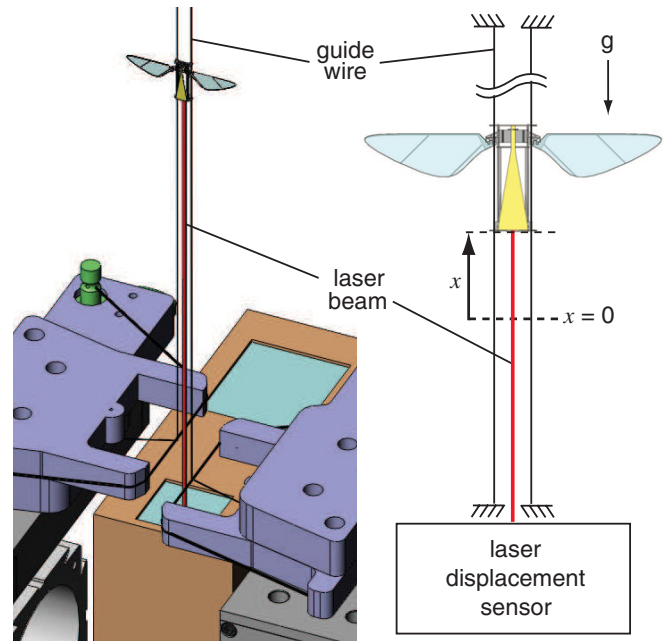


Figure 9. Setup used in the altitude control experiments. Left: isometric view. Right: front view.

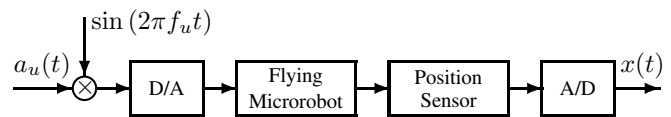


Figure 10. Block diagram of the system used in altitude control experiments.

measuring the altitude using a long-range laser displacement sensor, depicted in figure 9 and described in subsection 5.4. The altitude measurement is labeled as $x(t)$, which is the signal to be used in the implementation of feedback controllers, after being read by the laser position sensor and digitized using an analog-to-digital board, as described in figure 10. The reason for constraining the movement of the microrobot to one degree of freedom is that in the current design, the system is under-actuated, without the ability to completely control all body moments [17]. The input to the microrobot is a voltage to the piezoelectric actuator that provides mechanical power to the system. In figure 10, the block labeled as D/A represents the digital-to-analog signal conversion and the amplification to the analog range [0, 300] V from the range [0, 1] on which the digital signal $a_u(t)$ has been normalized. Note that the RMS values of the currents at 300 V range from 0.5 to 1 mA, approximately [23]. Thus, representing all the disturbances and sensor noise affecting the system by the output disturbance signal $d(t)$, the system illustrated in figure 9 and depicted in figure 10 can be idealized by the block diagram in figure 11.

Inspired not only by nature, but also for practical reasons, roboticists have commonly designed flapping-wing mechanisms to be excited by sinusoidal signals. Here, we adopt the same design choice, acknowledging that other shapes for exciting signals are conceivable. In this approach, formally,

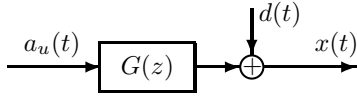


Figure 11. Idealized system dynamics. $G(z)$: discrete-time open-loop plant; $a_u(t)$: input amplitude; $x(t)$: measured altitude; $d(t)$: output disturbance, representing the aggregated effects of all the disturbances affecting the system, including stochastic wind currents. $G(z)$ is idealized under the assumption that the frequency f_u is fixed and that $a_u(t)$ oscillates around a_H , which is the exact amplitude required for hovering.

the input signals have the form

$$u(t) = a_u(t) \sin(2\pi f_u t). \quad (7)$$

The idea is to think of $\sin(2\pi f_u t)$ as a part of the system and consider $a_u(t)$ to be the control signal, generated according to some control law. Thus, in closed loop, the signal applied to the system in figure 11 has the form

$$a_u(t) = \begin{cases} 1 & \text{if } b_u(t) \geq 1 \\ b_u(t) & \text{if } \underline{a}_u < b_u(t) < 1 \\ \underline{a}_u & \text{if } b_u(t) \leq \underline{a}_u \end{cases} \quad (8)$$

with

$$b_u(t) = K(z)e_x(t), \quad (9)$$

where $K(z)$ is a discrete-time LTI operator depending on the delay operator z^{-1} and the real number $\underline{a}_u \in [0, 1]$ is the minimum allowable value that $a_u(t)$ can take. The signal $e_x(t)$ is the control error defined as $e_x(t) = x_d(t) - x(t)$, where $x_d(t)$ is the desired altitude and, as stated before, $x(t)$ is the measured altitude signal depicted in figure 9. In general, an appropriate $K(z)$ can be found experimentally, or designed using a model of the microrobot dynamics. The latter approach is pursued here, using an identified model $\hat{G}(z)$ of the idealized system dynamics $G(z)$ in figure 11, with the fixed frequency $f_u = 90$ Hz. The system identification is performed using the *n4sid* algorithm [22], after exciting the system with a *pseudo-random binary signal* (PRBS) [24]. A section of the employed PRBS is shown on the upper-left in figure 12. Note that as shown on the lower-left in figure 12, this chosen input causes the flying robot to maintain an altitude larger than zero during the whole identifying experiment, i.e. the identification is performed during flight. The resulting identified LTI model is shown on the left in figure 13. A closed-loop validation of the identified model is shown on the right in figure 12.

Note that the resulting model $\hat{G}(z)$ is only valid when the robotic insect is flying around a hovering point. This means that the input $a_u(t)$ is oscillating around a constant amplitude $a_H \in \mathbb{R}$, defined as the amplitude generating the exact average lift-force that balances gravity. Clearly, a_H must be thought of as an abstract artifact and not as a practical value, because the required value of $a_u(t)$ needed for hovering might vary over time, due to degradation of the robot, for example. Also note that the identified model in figure 13 is only valid for $f_u = 90$ Hz. It follows that if another f_u is chosen, another system

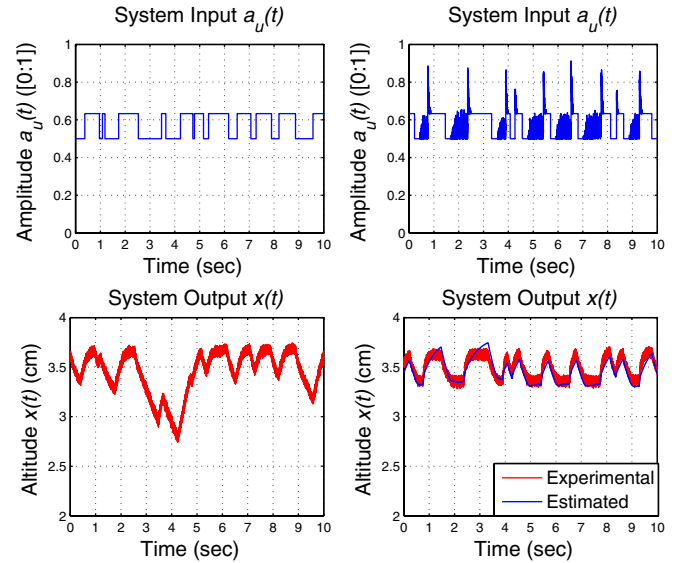


Figure 12. Excitation signals used in the system identification of $G(z)$, for $f_u = 90$ Hz. Left: section of the data used in the system identification of the system $G(z)$. Right: section of the data used in the validation of the identified model $\hat{G}(z)$ of $G(z)$.

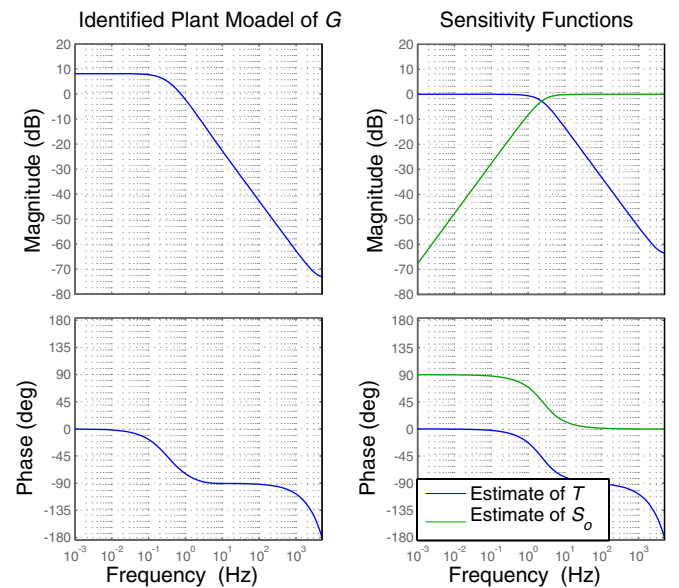


Figure 13. Left: Bode diagram of identified model $\hat{G}(z)$ of the plant $G(z)$. A 24th-order model was originally identified, a reduced second-order model, whose Bode plot closely matches the original 24-order model, is shown in blue. Right: estimate $\hat{S}_o = (1 + \hat{G}K)^{-1}$ of the output sensitivity function $S_o = (1 + GK)^{-1}$, shown in green. Estimate $\hat{T} = \hat{G}K(1 + \hat{G}K)^{-1}$ of the complementary sensitivity function $T = GK(1 + GK)^{-1}$, shown in blue.

identification has to be performed to represent the system associated with that specific frequency.

The methodology described in the previous paragraph treats the flying microrobot as a *black box*. In [25], in a qualitative analysis, the dynamics of insects is described as a black box that maps inputs to outputs. There, it is discussed that, using insects in free flight, the estimation of mappings have been attempted numerous times. However, this task is extremely difficult, because inputs cannot be arbitrarily

chosen by the experimenters and because the measurement of variables in free flight is very challenging. Fortunately, those are problems that are substantially more manageable in the case presented in this paper.

Using the model $\hat{G}(z)$ and classical techniques, the LTI controller $K(z)$ is designed. The stability and stability robustness of the closed-loop configuration under $K(z)$ is evaluated using the classical indices gain and phase margins, and the resulting performance can be predicted using estimates of the output and complementary sensitivity functions, $S_o = (1 + GK)^{-1}$ and $T = GK(1 + GK)^{-1}$ [26]. These estimates, computed as $\hat{S}_o = (1 + \hat{G}K)^{-1}$ and $\hat{T} = \hat{G}K(1 + \hat{G}K)^{-1}$, respectively, are shown on the right in figure 13. An important thing to note in figure 13 is that the identified model $\hat{G}(z)$ is a narrow-band low-pass filter that significantly amplifies and attenuates the low and high frequencies, respectively. This establishes fundamental constraints on the achievable speed of the robotic insect. Thus, the primary objectives of the controller design are to increase the system bandwidth and simultaneously to reject low-frequency disturbances. From the Bode plots of \hat{T} and \hat{S}_o , these objectives are achieved. The fulfillment of the first objective follows from noting that T maps the desired altitude signal $x_d(t)$ to the measured altitude signal $x(t)$, and that the bandwidth of \hat{T} is significantly wider than the bandwidth of \hat{G} . The fulfillment of the second objective follows from noting that in closed loop S_o maps the output disturbance $d(t)$ to the measured altitude $x(t)$, and that \hat{S}_o is a high-pass filter. The shapes of the resulting \hat{T} and \hat{S}_o are completely explained by the so-called waterbed effect, a direct consequence of the *Bode sensitivity integral theorem* [26].

3. Results

The purpose of this section is to demonstrate the capability of the robotic insect to perform hovering, trajectory-following and to reject disturbances, when connected in closed loop with the nonlinear controller defined by (8) and (9), as described in the previous section. The first two capabilities are demonstrated in figure 14, with $\underline{a}_u = 0.5$, and the third is demonstrated in figure 16, with $\underline{a}_u = 0.35$. A compressed visual description of the achieved results is given in the supplemental movie S1 (available at stacks.iop.org/BB/6/036009/mmedia). Additional details about the experiment in figure 14 are given in the supplemental movie S2 (available at stacks.iop.org/BB/6/036009/mmedia) and in figure 15. In the experiment in figure 14, the microrobot starts flapping at $time = 0$ s when the value of the signal $a_u(t)$ is slowly increased from 0 to 0.5. From the information in figures 6 and 8, it is clear that the lift-force produced with $a_u(t) = 0.5$ is not enough to produce a vertical movement. At $time = 10$ s the feedback loop is closed, and immediately the value of $a_u(t)$ reaches the allowed upper bound of 1, and as predicted by figure 8, the robotic insect starts to move vertically, reaching the desired position $x_d(t) = 2.5$ cm in 0.36 s, hovering at this position for 10 s. This transition is shown in the sequence of photographs in figure 16. Then, at $time = 20$ s, the desired position is set to $x_d(t) = 3.5$ cm.

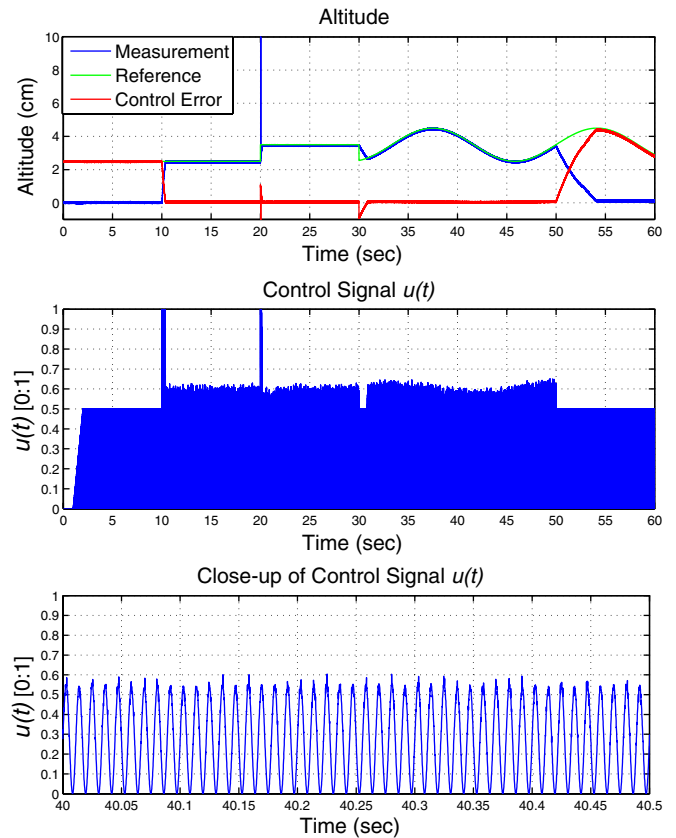


Figure 14. Stable hovering and trajectory following experiment. Upper plot: altitude measurement $x(t)$, reference $x_d(t)$ and control error $e_x(t)$. Middle plot: control signal $u(t) = \underline{a}_u(t) \sin(2\pi f_u t)$, with $\underline{a}_u = 0.5$. Bottom plot: close-up of control signal $u(t)$.

As can be observed in the supplemental movie S2 (available at stacks.iop.org/BB/6/036009/mmedia), the transition from 2.5 cm to 3.5 cm is both fast and smooth, despite the fact that due to a brief misalignment of the laser position sensor, the altitude information is erroneous for fractions of a second (the spike in the measurement trace at 20 s in the upper plot of figure 14). This empirically demonstrates the robustness of the proposed control strategy. Note that sensor spikes can be completely avoided by carefully aligning the laser position sensor under the microrobot.

The tracking capability of the employed control scheme is demonstrated in the second part of the same experiment. At $time = 30$ s, the reference is switched from the constant $x_d(t) = 3.5$ cm to the oscillatory signal $x_d(t) = [3.5 + \sin(2\pi \cdot 0.03t)]$ cm. From (8), the maximum speeds at which the microrobot can travel upward and downward are determined by the mass of the robotic insect and by the upper and lower bounds on $a_u(t)$, 1 and 0.5, respectively. The upper bound is a hard constraint corresponding to the maximum voltage to which the piezoelectric actuator can be safely excited. The lower bound is a design choice that can take values in the interval $[0, 1]$. Figure 15 demonstrates the disturbance rejection capabilities of the proposed strategy. Here, the hovering microrobot is disturbed by air gusts using a small hose. The video of the complete experiment is shown in the supplemental movie S3 (available at stacks.iop.org/BB/6/036009/mmedia). Note that

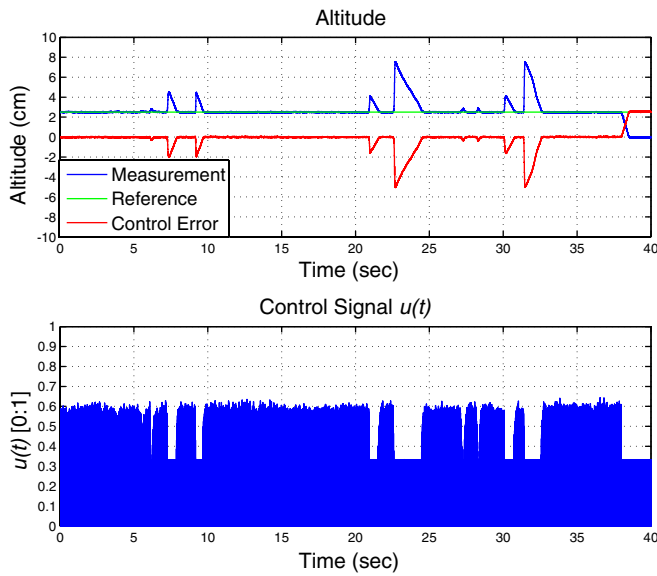


Figure 15. Disturbance rejection experiment. Upper plot: altitude measurement $x(t)$, reference $x_d(t)$ and control error $e_x(t)$. Bottom plot: control signal $u(t) = a_u(t) \sin(2\pi f_u t)$, with $a_u = \frac{1}{3}$. Each spike corresponds to a disturbance event.

as is clear from the lower plot in figure 15, in this case, $a_u = \frac{1}{3}$, which decreases the system’s reaction-time when it is required to move downward at high speeds. Additional trajectory following experiments are presented in the supplemental materials (available at stacks.iop.org/BB/6/036009/mmedia). There, movie S1 gives an overview of the control system capabilities, movie S4 shows the trajectory following of a higher-frequency sinusoidal signal, and movie S5 shows the trajectory following of a square wave.

4. Discussion and conclusion

The aerodynamics of natural flying insects is highly complex and the precise mechanisms by which they are able to propel themselves is not yet completely understood [27]. Also, as discussed in [16], the analysis of the aeromechanics of passive rotation of even simple flapping mechanisms yields a highly nonlinear dynamic description of the associated phenomena. Here, adopting the *ceteris paribus* principle, we concerned ourselves with the altitude control problem in one degree of freedom. In this context, we empirically show that substantial information about the flying system can be gathered from input–output experiments, so that robust controllers can be designed to achieve tasks such as

hovering, trajectory following and rejection of disturbances. This follows from adopting suitable and effective design paradigms such as considering the exciting signal in figure 10 as part of a linear system that can be identified using standard state-space system identification algorithms. The results presented here suggest that the approach introduced in this investigation is appropriate in the pursuit of completely autonomous flying microrobots. It is possible to envision the application of the same design principles and analytical tools to more sophisticated flying micromachines, capable of generating actuation in more than one degree of freedom [17]. The feasibility of integrating additional actuators in the design of the microrobot is supported by the information in figure 8, which indicates that if the right exciting signals are chosen, the flying microrobot can carry as much as 3.6 times its current weight. Beyond the findings relevant from an engineering perspective, the results presented here could have an important significance from a biological perspective, since they unequivocally demonstrate that stable hovering and vertical trajectory following can be achieved without the need for active control over wing pronation and supination.

5. Materials and methods

5.1. Fabrication of the robotic insect

The robotic insect used in this research was entirely developed and fabricated by the authors at the Harvard Microrobotics Laboratory, based upon designs which previously demonstrated the ability to liftoff [1]. The key components include a piezoelectric bending bimorph cantilever actuator [28], a flexure-based transmission, a pair of airfoils, and an airframe which serves as a mechanical ground. The transmission maps the approximately linear motions of the actuators into the flapping motion of the wings. The transmission consists of links and joints with geometries designed to maximize the product of stroke amplitude and first resonant frequency, given known actuator and airfoil properties. Fabrication of all components relies on a layered meso-scale manufacturing process which starts with thin sheets of the constituent materials that are laser micromachined into desired 2D geometries [29]. Actuators are created by laminating two piezoelectric plates (PZT-5H from Piezo Systems, Inc.) to a carbon fiber spacer and electrode layer. The airframe and transmission are created by layering a 7.5 μm polyimide film (Chemplex Industries) with carbon fiber face sheets. By appropriate design of the layer geometries, any 3D structure can be created in this manner including flexure-based articulated components and

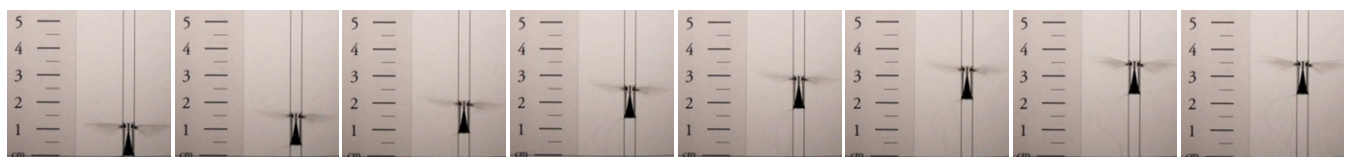


Figure 16. Video sequence showing the transition from 0 to 2.5 cm in figure 14. The side ruler is placed as a rough reference, not for exact measurement of the flying robot’s altitude. The exact vertical position $x(t)$ is measured using the laser displacement sensor depicted in figure 9. The sampling time at which the frames were taken is approximately 51.4 ms.

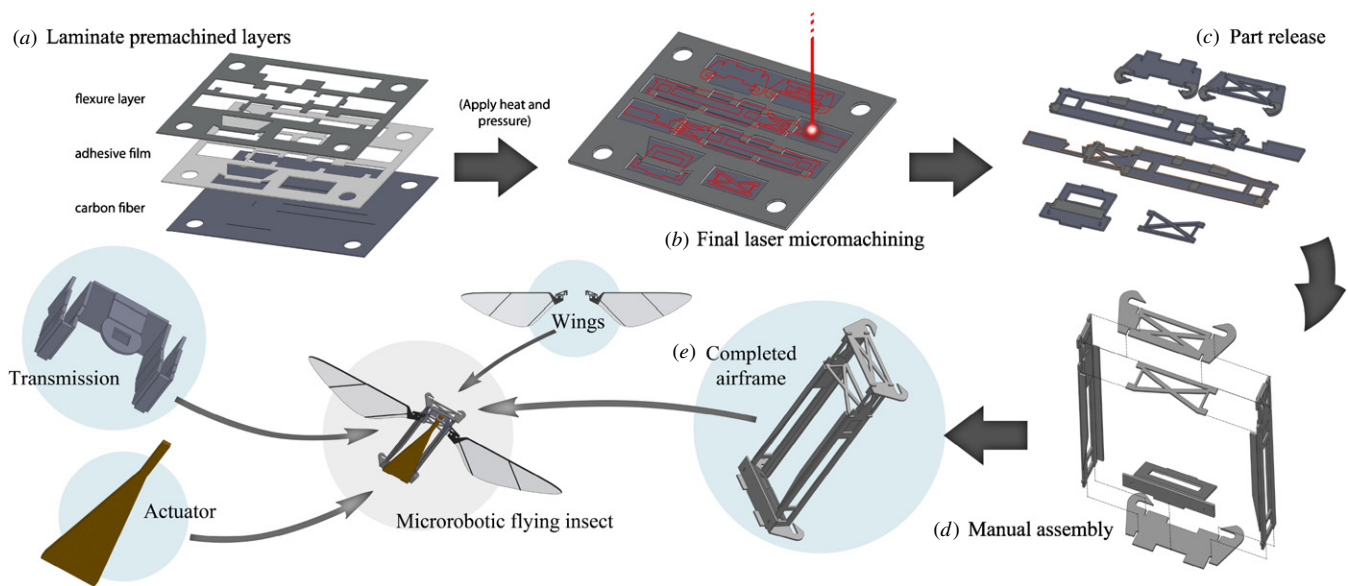


Figure 17. Graphical description of the fabrication and assembling process. The whole process is composed of four main steps: lamination (a), singulation (b), release (c) and assembly (d).

rigid structures (e.g. the transmission and the airframe, respectively). A final manual assembly step is required to integrate all components and make electrical connections to the actuator.

The main difference between the previous robotic insect designs and the one utilized in this research is the addition of hooks to the airframe for compatibility with the experimental setup in figure 9. The fabrication and assembling process of the airframe is shown in figure 17. The other components of the microrobot are fabricated in a very similar manner, and assembled as shown in figure 17.

5.2. System identification of plants P and G

As indicated in the main text, both plants P and G are identified using the $n4sid$ algorithm in Matlab. The acronym $n4sid$ stands for numerical algorithm for subspace state space identification [22].

5.3. Digital processing of the signals

The real-time processing of all the signals involved is done using a *MathWorks* xPC-Target system. The sampling-and-hold rate used for measuring and control was set at 10 kHz.

5.4. Sensors

The displacement of the actuator, depicted in figure 4, is measured using a short-range CCD laser displacement sensor LK-2001 fabricated by Keyence. The altitude of the robotic insect, depicted in figure 9, is measured using a long-range CCD laser displacement sensor LK-2503 fabricated by Keyence. In the static flapping experiments in figure 4, the instantaneous force is measured by sensing the deflection of the double-cantilever beam to which the microrobot is rigidly connected. The beam deflection is measured using a capacitive

displacement sensor. For details on the design of the force sensor, see [20].

Acknowledgments

This work was funded in part by the Office of Naval Research (award number N00014-08-1-0919-DOD35CAP), the National Science Foundation (award number CCF-0926148) and the Wyss Institute for Biologically Inspired Engineering. Any opinions, findings, and conclusions or recommendations expressed in this material are those of the authors and do not necessarily reflect views of the National Science Foundation.

References

- [1] Wood R J 2008 The first takeoff of a biologically inspired at-scale robotic insect *IEEE Trans. Robot.* **24** 341–7
- [2] Zbikowski R 2004 Sensor-rich feedback control: a new paradigm for flight control inspired by insect agility *IEEE Instrum. Meas. Mag.* **7** 19–26
- [3] Sherman A and Dickinson M H 2003 A comparison of visual and haltere-mediated equilibrium reflexes in the fruit fly *Drosophila melanogaster* *J. Exp. Biol.* **206** 295–302
- [4] Frye M A and Dickinson M H 2001 Fly flight: a model for the neural control of complex behavior *Neuron* **32** 385–8
- [5] Tammero L F, Frye M A and Dickinson M H 2004 Spatial organization of visuomotor reflexes in *Drosophila* *J. Exp. Biol.* **207** 113–22
- [6] Tammero L F and Dickinson M H 2002 The influence of visual landscape on the free flight behavior of the fruit fly *Drosophila melanogaster* *J. Exp. Biol.* **205** 327–43
- [7] Deng X, Schenato L, Wu W C and Sastry S S 2006 Flapping flight for biomimetic robotic insects: part I. System modeling *IEEE Trans. Robot.* **22** 776–88
- [8] Deng X, Schenato L and Sastry S S 2006 Flapping flight for biomimetic robotic insects: part II. Flight control design *IEEE Trans. Robot.* **22** 789–803
- [9] Doman D B, Oppenheimer M W and Sigthorsson D O 2010 Wingbeat shape modulation for flapping-wing

- micro-air-vehicle control during hover *J. Guid. Control Dyn.* **33** 724–39
- [10] Pérez-Arancibia N O, Whitney J P and Wood R J 2011 Lift force control of flapping-wing microrobots using adaptive feedforward schemes *IEEE/ASME Trans. Mechatron.* at press
- [11] Pérez-Arancibia N O, Whitney J P and Wood R J 2011 Lift force control of a flapping-wing microrobot *Proc. 2011 Am. Cont. Conf. (San Francisco, CA)* pp 4761–8
- [12] Lehmann F-O and Dickinson M H 1998 The control of wing kinematics and flight forces in fruit flies (*Drosophila* spp.) *J. Exp. Biol.* **201** 385–401
- [13] Altshuler D L, Dickson W B, Vance J T, Roberts S P and Dickinson M H 2005 Short-amplitude high-frequency wing strokes determine the aerodynamics of honeybee flight *Proc. Natl Acad. Sci.* **102** 18213–8
- [14] Ennos A R 1988 The importance of torsion in the design of insects wings *J. Exp. Biol.* **140** 137–60
- [15] Young J, Walker S M, Bomphrey R J, Taylor G K and Thomas A L R 2009 Details of insect wing design and deformation enhance aerodynamic function and flight efficiency *Science* **325** 1549–52
- [16] Whitney J P and Wood R J 2010 Aeromechanics of passive rotation in flapping flight *J. Fluid Mech.* **660** 197–220
- [17] Finio B M and Wood R J 2010 Distributed power and control actuation in the thoracic mechanics of a robotic insect *Bioinspir. Biomim.* **5** 045006
- [18] Ellington C P 1984 The aerodynamics of hovering insect flight. VI. Lift and power requirements *Phil. Trans. R. Soc. B* **305** 145–85
- [19] Weis-Fogh T 1973 Quick estimates of flight fitness in hovering animals, including novel mechanisms for lift production *J. Exp. Biol.* **59** 169–230
- [20] Wood R J, Cho K-J and Hoffman K 2009 A novel multi-axis force sensor for microrobotics applications *Smart Mater. Struct.* **18** 125002
- [21] Wood R J, Steltz E and Fearing R S 2005 Nonlinear performance limits for high energy density piezoelectric bending actuators *Proc. IEEE Int. Conf. Robot. Autom. (Barcelona, Spain)* pp 3633–40
- [22] Van Overschee P and De Moor B 1996 *Subspace Identification for Linear Systems* (Boston, MA: Kluwer)
- [23] Karpelson M, Wei G Y and Wood R J 2009 Milligram-scale high-voltage power electronics for piezoelectric microrobots *Proc. IEEE Int. Conf. Robot. Autom. (Kobe, Japan)* pp 2217–24
- [24] Ljung L 1999 *System Identification* (Upper Saddle River, NJ: Prentice-Hall)
- [25] Taylor G K 2001 Mechanics and aerodynamics of insect flight control *Biol. Rev.* **76** 449–71
- [26] Skogestad S and Postlethwaite I 1996 *Multivariable Feedback Control* (Chichester: Wiley)
- [27] Dudley R 2000 *The Biomechanics of Insect Flight* (Princeton, NJ: Princeton University Press)
- [28] Wood R J, Steltz E and Fearing R S 2005 Optimal energy density piezoelectric bending actuators *Sensors Actuators A* **119** 476–88
- [29] Wood R J, Avadhanula S, Sahai R and Fearing R S 2008 Microrobot design using fiber reinforced composites *J. Mech. Des.* **130** 052304